


Dynamic modeling and experimental evaluation of a constant-force dielectric elastomer actuator

Journal of Intelligent Material Systems
and Structures
0(0) 1–13
© The Author(s) 2012
Reprints and permissions:
sagepub.co.uk/journalsPermissions.nav
DOI: 10.1177/1045389X12457251
jim.sagepub.com


Giovanni Berselli¹, Rocco Vertechy², Mitja Babič³ and Vincenzo Parenti Castelli⁴

Abstract

Constant-force actuators based on dielectric elastomers can be obtained by coupling a dielectric elastomer film with particular compliant frames whose structural properties must be carefully designed. In any case, the practical achievement of a desired force profile can be quite a challenging task owing to the time-dependent phenomena, which affect the dielectric elastomer's electromechanical response. Within this scenario, a hyperviscoelastic model of a rectangular constant-force actuator is reported. The model, based on the bond graph formalism, can be used as an engineering tool when designing and/or controlling actuators that are expected to work under given nominal conditions. Simulations and experimental results are provided, which predict the system response to fast changes in activation voltage and actuator position as imposed by an external user.

Keywords

dielectric elastomer actuator, quasi-linear viscoelasticity, bond graph modeling

Introduction

The interest in linear actuators based on dielectric elastomers (DEs) is currently increasing. Potential applications span bioinspired robotics (Carpi et al., 2008; Kim and Tadokoro, 2007), medical engineering (Biddiss and Chaua, 2007), active vibration damping (Kaal and Herold, 2011), and haptic rendering for immersive virtual reality (Zhang et al., 2006). Recent researches have also explored the potentials of DE-based variable stiffness devices (Berselli et al., 2012; Dastoor and Cutkosky, 2012) for safe human-machine interaction (Bicchi, 2008; Palli et al., 2011; Palli and Melchiorri, 2011).

For actuation usage, DEs are shaped in thin films that are first prestretched and then coated with compliant electrodes to form an electrically deformable film (EDF). Activation of the EDF via the placement of large electric potential differences (voltages) between the electrodes can induce film area expansion, and thus points' displacements, which can be used to produce useful mechanical work (whenever forces are applied to such points).

Several kinds of DE actuators have been proposed in the literature, characterized by various shapes/sizes and disparate performances in terms of efficiency, force/power densities, and reliability (see O'Halloran et al., 2008 for a review). Despite these differences, a typical DE actuator is composed of a mono- or multilayered

EDF, which provides electromechanical energy conversion, an energy source that delivers the electric activation stimuli, and a passive flexible frame that might be necessary to support the EDF.

As previously shown in the literature, particular EDF shapes with proper prestretches (see, for example, the lozenge-shaped actuator proposed by Vertechy et al. (2010)) or particular compliant frames (see, for example, Berselli et al., 2009, 2011b; Pedersen et al., 2006; Wingert et al., 2006) can be used to conceive mono- or bidirectional actuators characterized by a constant available thrust over a given range of motion. Constant-force actuators are typically desirable since they possess uniform behavior, enable optimal use of the available output work, and are easy to control (Hackl et al., 2005; Huber et al., 1997). Nonetheless, the practical achievement of a desired force profile is

¹DIEF—University of Modena and Reggio Emilia, Modena, Italy

²PERCRO Lab—Scuola Superiore Sant'Anna, Pontedera, Italy

³Department of Automation, Biocybernetics and Robotics, Jožef Stefan Institute, Ljubljana, Slovenia

⁴DIEM—University of Bologna, Bologna, Italy

Corresponding author:

Giovanni Berselli, University of Modena and Reggio Emilia, Via Vignolesse 905, 41125 Modena, Italy.

Email: giovanni.berselli@unimore.it

challenging as long as the actuator response is highly affected by creep and stress-relaxation effects, which are intrinsic of the nonlinear viscoelastic nature of the employed DE material. Hence, reliable dynamic models are needed to correctly predict the time-dependent phenomena arising during the actuator functioning.

Within this scenario, the objective of this article is to investigate the dynamic properties of a constant-force actuator of rectangular shape whose conceptual design is reported in Berselli et al. (2009).

Figure 1(a) and (b) represents the actuator in deactivated (OFF) and activated (ON) states, respectively. The actuator frame (Figure 1(c)), whose pseudo-rigid model schematic (Howell, 2001) is depicted in Figure 1(d), is a fully compliant 6-bar linkage mechanism. The EDF, shaped as a rectangle (Figure 1(c)), is attached to link 1 (base link) and link 2 (moving platform). Displacement along the y -direction (as well as, alternatively, rotation) is prevented by the symmetry of both the 6-bar linkage geometry and the EDF stress distribution so that links 1 and 2 are always parallel to each other. Half frame can then be schematized as a slider crank compliant mechanism (SCCM) (Figure 1(d)) whose elastic properties allow to achieve the desired constant force (refer to Berselli et al., 2011b for a detailed description). The frame prototype is shown in Figure 2(a) (undeflected condition) and in Figure 2(b) (moving platform loaded with a constant load acting in the x -direction). The elastic joints are made with a couple of close-wound helical springs (Figure 3(a)), which allow large rotations while preventing fatigue failures and excessive external size (Lotti et al., 2006). In fact, when the springs are subjected to an adequate bending moment (principal load, Figure 3(b)), the deformation is distributed all along a helical beam such that a limited number of coils can easily generate a substantial displacement. At the same time, parasitic effects (i.e. undesired motions) are reduced thanks to a higher stiffness with respect to load components other than the principal

bending moment. The overall actuator prototype is depicted in Figure 2(c) (actuator deactivated state) and in Figure 2(d) (actuator activated state).

Following previous studies on piezoelectric actuators (Rodriguez-Fortun et al., 2010), the model presented in this article is based on bond graph (BG) formalism (whose advantages are described in, for example, Karnopp et al., 2005) and includes a description of the electrostatic, hyperviscoelastic behavior of the EDF (Goulbourne et al., 2007; Michel et al., 2010; Plante and Dubowsky, 2007; Wissler, 2007) connected to an ideal high-voltage (HV) power supply (Hackl et al., 2005; Zhang et al., 2006). Different from preceding studies, the force contribution of the compliant frame is hereafter included. Simulations and experimental results are provided, which predict the system response to fast changes in activation voltage and actuator position as imposed by an external user.

Background on rectangular constant-force actuators

Achievement of a constant available thrust

Let us first neglect any time-dependent phenomena that might arise during actuator functioning. Recalling general guidelines reported in Berselli et al. (2009), it can be stated that the EDF deformation produces a variation of the actuator length $x = |(P - O)|$, where P and O are, for instance, two points of the actuator lying on the EDF axis of symmetry (Figure 1(d)), and a force having the same direction as vector \overline{OP} that can be supplied to an external user. This force, called the actuator available thrust, F_a , is generally given by the sum of two contributions: the frame reaction force, F_s , due to the frame own stiffness, and the EDF force, F_f , that is the resultant force in the direction of actuation due to the stress field arising in the EDF. The force F_f decreases in modulus upon EDF activation. In particular, according to a one-dimensional model, the EDF behaves as a nonlinear tension spring with stiffness

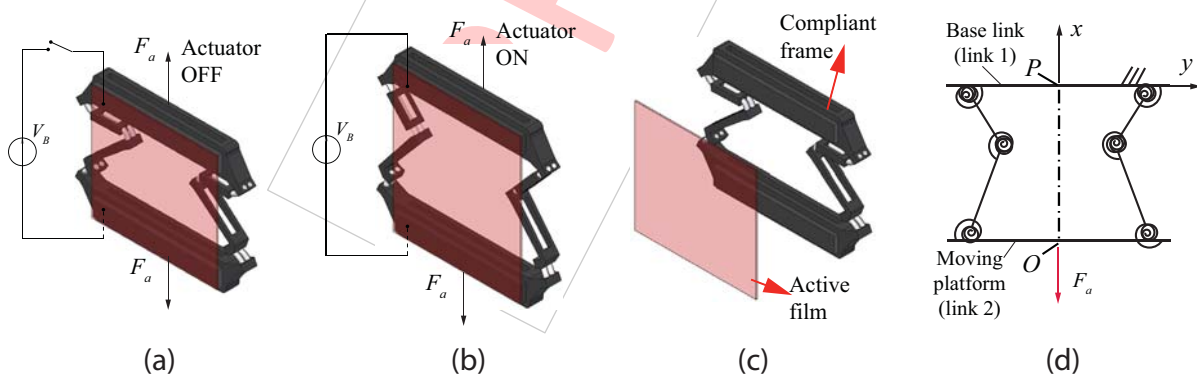


Figure 1. Concept behind the proposed solution and actuator 3D model, (a) deactivated state, (b) activated state, (c) assembly exploded view, (d) and compliant frame schematic.

3D: three-dimensional.

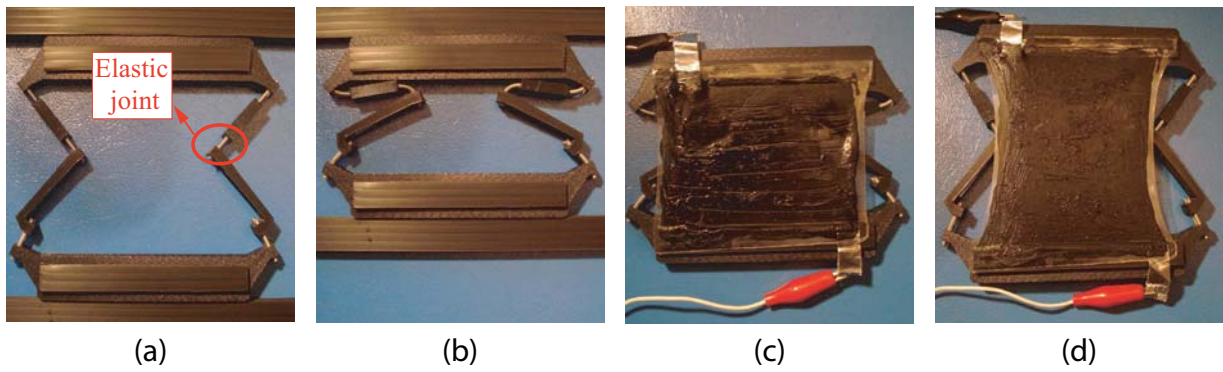


Figure 2. Actuator prototype. Frame prototype (a) in undeflected condition and (b) under constant external load application and actuator in (c) deactivated and (d) activated states.

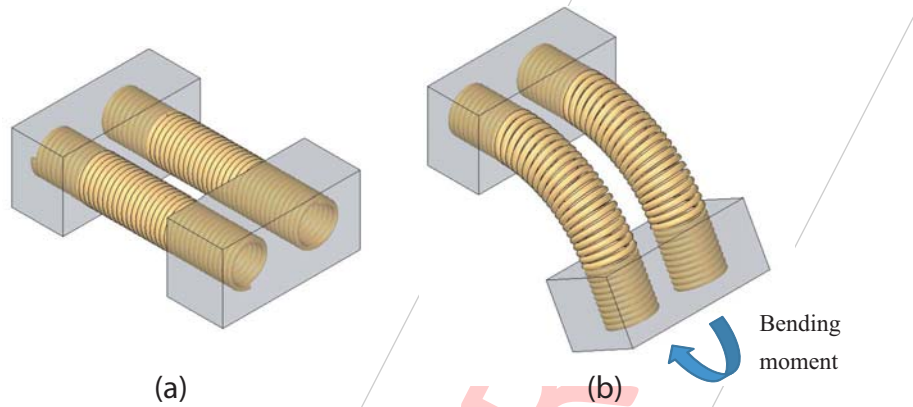


Figure 3. Elastic joint (Figure 2(a)) made with closed-wound helical springs: (a) undeflected condition and (b) deflected condition when subjected to principal load.

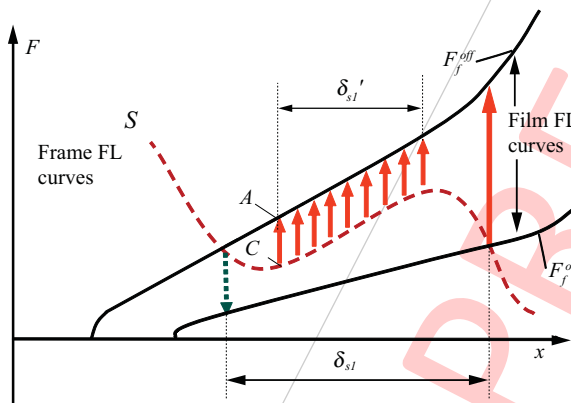


Figure 4. FL curves qualitatively showing the moduli of F_f and F_s and the “negative stiffness” effect. FL: force–length.

$K_f = dF_f/dx$, whereas the flexible frame behaves as a nonlinear compression spring with stiffness $K_s = dF_s/dx$ and coupled in parallel with the EDF.

Figure 4 shows qualitative diagrams of force–length (FL) curves concerning the moduli of F_f and F_s . In particular, the *continuous* curves F_f^{off} and F_f^{on} represent

the film force F_f when the EDF is deactivated (OFF-state mode) or activated (ON-state mode), respectively. The *dotted* curve S represents the modulus of the frame reaction force F_s .

Assuming the EDF electromechanical characteristics as given, a constant-force actuator can be obtained by coupling the EDF with particular compliant mechanisms (as, for instance, the SCCM), which are designed so as to provide a negative elastic reaction force that increases in modulus as the actuator length x increases (i.e. $K_s < 0$). As an example, considering a frame having the FL profile represented by the curve S , for a consistent part of the stroke (namely, δ'_{s1}), F_a maintains a constant value, F_a^{off} , equal to the distance \overline{AC} as the actuator is in its OFF-state. In this case, the overall actuator stroke, δ_{s1} , can be limited by means of mechanical stops in order to prevent its functioning in regions where F_a^{off} is not constant.

Constant-force actuator production steps

Figure 5 summarizes the conceptual steps carried out for the production of the planar DE actuator with

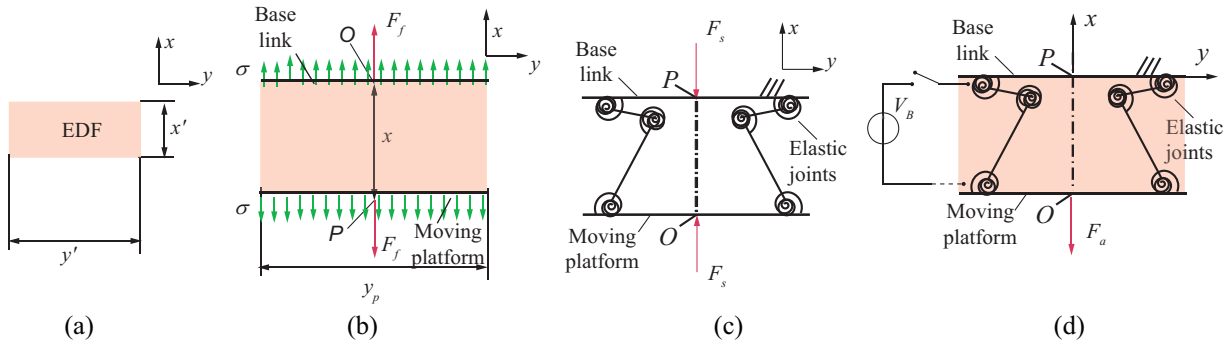


Figure 5. Rectangular actuator production steps. (a) Unstretched EDF, (b) prestretched EDF, (c) precompressed frame, and (d) rectangular actuator, OFF-state mode. EDF: electrically deformable film.

rectangular geometry depicted in Figure 2. An undeformed EDF (reference configuration, Figure 5(a)) is prestretched along the length (x -direction) and width (y -direction, Figure 5(b)). In parallel, the fully compliant frame is precompressed (Figure 5(c)). The EDF is then glued to the frame's fixed link and moving platform. In such a way, the imposed EDF prestretch along the width direction is completely maintained. Starting from this unloaded configuration (actuator OFF-state mode, Figure 5(d)), activation of the EDF by means of a HV source can induce a film expansion along the EDF unconstrained direction, x (Figure 1(a) and (b)). In particular, as deeply described in Berselli et al. (2011b), a suitable design of the frame link lengths and elastic joints stiffness allows to tailor the overall actuator stiffness to the specific application and, in particular, to achieve the desired constant force.

Description of the actuator lumped parameter model

For design purposes, DEs can be considered as incompressible, hyperelastic linear dielectrics whose electric polarization is fairly independent of material deformation (Kornbluh et al., 1995; Pelrine et al., 1998). Neglecting thermally induced deformations (Vertechy et al., in press), the coupled electromechanical response of the DE actuator portrayed in Figure 1 can then be represented and understood via the one-dimensional lumped electrical and mechanical models depicted in Figure 6. With reference to Figure 6(a) and similarly to Babic et al. (2010), the electrical system comprises the following:

- An ideal HV power supply;
- An EDF electrical model, which is composed of—
 - A variable capacitance $C_{DE} = C_{DE}(x)$ depending on the actuator configuration x ;

- The lumped EDF electrode resistance R_e (assumed constant);
- The lumped resistance R_l accounting for the leakage current flowing through the EDF (assumed constant).

With reference to Figure 6(b), the mechanical system comprises the following:

- An electrically induced term, F_{em} , representing the EDF electromechanical coupling and having the dimension of a force. The force F_{em} is assumed dependent on the actuator position x , on the applied voltage V , and on the absolute dielectric permittivity of the DE, ϵ ;

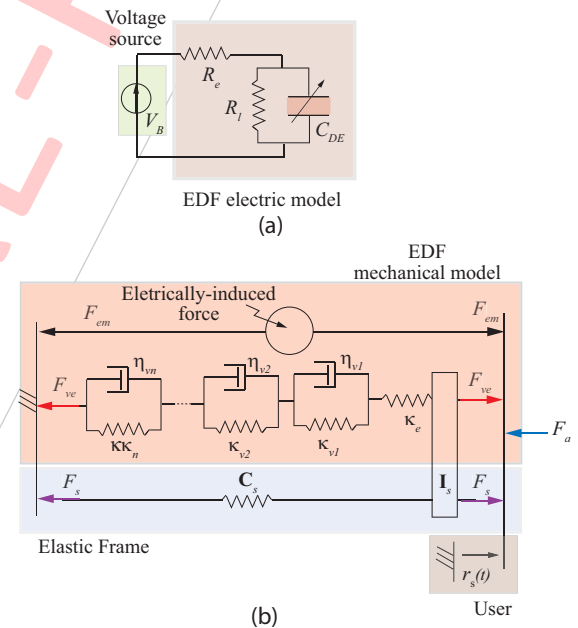


Figure 6. Electrical and mechanical model of a DE actuator. (a) Electrical model and (b) mechanical model. DE: dielectric elastomer; EDF: electrically deformable film.

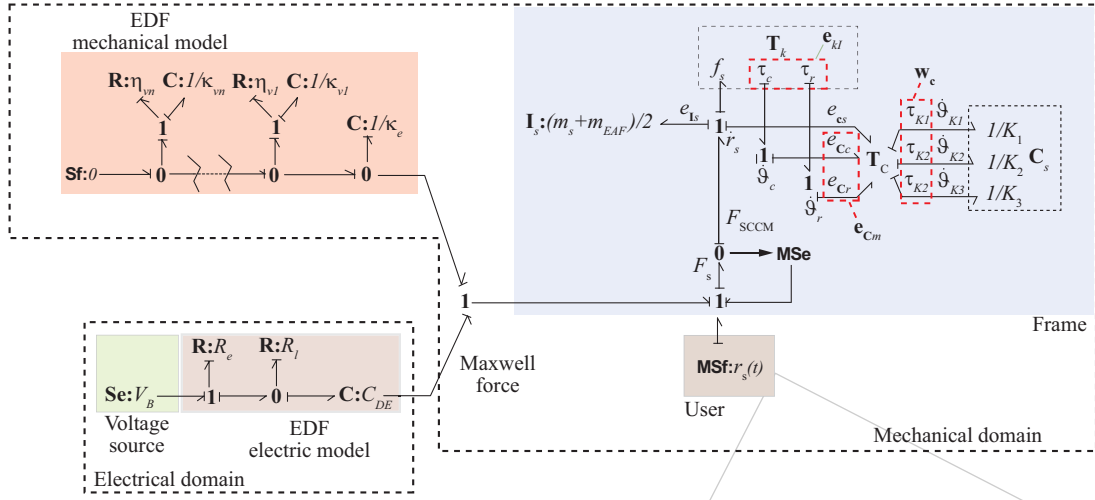


Figure 7. Bond graph of a DE actuator.

- An internal nonconservative force, F_{ve} , accounting for the purely elastic and viscoelastic effects within the EDF and described by means of a quasi-linear viscoelastic (QLV) model (Findley et al., 1989; Fung, 1993). According to the QLV assumptions, the force F_{ve} depends on the EDF constitutive parameters and on the actuator position x , and velocity \dot{x} , that is, $F_{ve}(x, \dot{x})$;
- An internal conservative force, F_s , due to the frame's stiffness and inertia. The force F_s is function of the actuator's output position x , and acceleration \ddot{x} , that is $F_s(x, \ddot{x})$, as well as of the masses of the moving links and of the stiffness of the compliant joints. The EDF masses are assumed rigidly connected to the frame moving platform.

The BG model of the overall system with causality assignment is depicted in Figure 7 where the system components' interconnection is highlighted. In particular, thanks to the particular actuator geometry, analytical expression of the system forces can be derived.

Mathematical model of the DE film force

Concerning EDF kinematics, let us define $\lambda_i (i = x, y, z)$ as the principal stretches, and x' and y' as the EDF planar dimensions in the reference configuration (unstretched EDF, Figure 5(a)), whereas x and y_p are the EDF planar dimensions in the actual configuration (Figure 5(b) and (d)). As said, y_p remains constant during actuator functioning along with the principal pre-stretch λ_p applied in the y -direction. Assuming EDF incompressibility ($\lambda_x \lambda_y \lambda_z = 1$), the EDF deformation state (pure shear deformation²) is characterized by the following principal stretches

$$\lambda_x = \lambda = \frac{x}{x'}; \quad \lambda_y = \lambda_p = \frac{y_p}{y'}; \quad \lambda_z = \frac{1}{\lambda_x \lambda_y} = \frac{z}{z'} \quad (1)$$

EDF electrical model

From the electrical standpoint, the EDF can be modeled as a planar capacitor such that

$$C_{EDF}(x) = \varepsilon \frac{y_p x}{z} = \varepsilon \frac{y_p \lambda_p}{z' x'} x^2 \quad (2)$$

$$= \bar{C}_{EDF} \left(\frac{x}{x'} \right)^2 \quad (3)$$

where $\varepsilon = \varepsilon_0 \varepsilon_r$, $\varepsilon_0 = 8.85e^{-12} \text{ F/m}$ is the dielectric constant of the vacuum, and $\varepsilon = 4.5$ is the absolute dielectric permittivity of the DE. The constant term \bar{C}_{EDF} is the minimum EDF capacitance achieved for $x = x'$. Given an ideal voltage source V_B , the time derivative of the electric charge stored on the EDF electrode surface can be derived directly from the BG of Figure 7. In particular, the following expression holds

$$\dot{q}_{DE} = \frac{V_B}{R_E} - \frac{q_{DE}}{C_{DE}(x)} (R_E^{-1} + R_L^{-1}) \quad (4)$$

EDF electromechanical coupling

The expression of the overall external force F_f that must be supplied at O and P (and directed along the line joining these points) to balance the EDF stress field at a given (fixed) generic configuration x of the actuator is given by

$$\begin{aligned} F_f &= zy_p \sigma \\ &= \underbrace{zy_p (\sigma_{ve})}_{F_{ve}} + \underbrace{zy_p (\sigma_{em})}_{F_{em}} \end{aligned} \quad (5)$$

where σ is the stress on the DE film cross section (also depicted in Figure 5(b)). Similar to Goulbourne et al. (2007), the stress σ is assumed to be the sum of a viscoelastic stress σ_{ve} and an “electrically induced” term σ_{em} (referred in the literature as *Maxwell stress*; Goulbourne et al., 2007). Accordingly, the overall force $F_f = F_f(x, \dot{x}, V)$ is then split into a viscoelastic component F_{ve} and an electrically induced term F_{em} , having the dimension of a force and usually referred to as *Maxwell force* (Kofod, 2008; Plante and Dubowsky, 2007).

Owing to the simple actuator shape, as demonstrated in (Kofod, 2008), the term σ_{em} can be written as

$$\sigma_{em} = -\varepsilon \left(\frac{V_{DE}}{z} \right)^2 = -\varepsilon \left(\frac{q_{DE}}{zC_{DE}} \right)^2 = -\frac{q_{DE}^2}{\varepsilon y_p^2 x^2} \quad (6)$$

where the relation $V_{DE} = q_{DE}/C_{DE}$ and equation (2) have been applied. The term F_{em} is then given by

$$F_{em} = -\frac{x' z' q_{DE}^2}{\varepsilon \lambda_p y_p x^3} \quad (7)$$

EDF viscoelastic behavior

As previously stated, the EDF mechanical behavior is affected by relevant time-dependent phenomena (such as hysteresis, creep, and stress relaxation). In general, the EDF behaves nonlinearly, and three-dimensional viscoelastic models suitable for finite deformations should be employed (Holzapfel, 2001). Nonetheless, simpler assumptions are sometimes necessary for model-based control of DE actuators (Xie et al., 2005). In some cases, under restricted range of the involved variables, the linear theory may be applied. Within the linear framework, the stress is proportional to the displacement at a given time, and the linear superposition principle holds. Several models, being composed of linear springs and linear viscous dampers arranged in different configurations have been proposed in the literature (Findley et al., 1989; Fung, 1993). As an instance, a Kelvin model consists of a parallel spring–damper system, whereas the standard linear viscoelastic solid model, shown in Figure 8 and also named *Zener model*, is composed of a linear spring connected in series to the

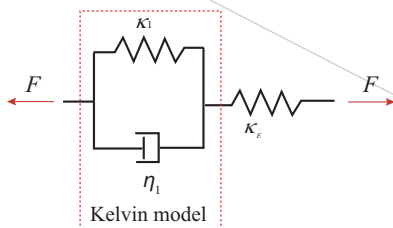


Figure 8. Standard linear viscoelastic solid model.

forementioned Kelvin model. In this latter case, stress and strain are related through the following differential equation

$$\sigma_{ve} + \frac{\eta}{\kappa_1 + \kappa_2} \dot{\sigma}_{ve} = \frac{\kappa_1}{\kappa_1 + \kappa_2} (\kappa_2 \varepsilon + \eta \dot{\varepsilon}) \quad (8)$$

Equation (8) can be solved with respect to the strain $\varepsilon(t)$ or with respect to the stress $\sigma_{ve}(t)$ by considering a constant input stress, $\sigma_{ve,0}$, or a constant input strain, ε_0 , respectively, and assuming in both cases the initial conditions equal to zero. In such a case, one obtains:

$$\varepsilon(t) = \hat{\mathcal{J}}(t) \cdot \sigma_{ve,0} = \left[\frac{1}{\kappa_1} + \frac{1}{\kappa_2} \left(1 - e^{-\frac{\kappa_2}{\eta} t} \right) \right] \cdot \sigma_{ve,0} \quad (9)$$

$$\sigma_{ve}(t) = \hat{\mathcal{K}}(t) \cdot \varepsilon_0 = \frac{\kappa_1}{\kappa_1 + \kappa_2} \left(\kappa_2 + \kappa_1 \cdot e^{-\frac{\kappa_1 + \kappa_2}{\eta} t} \right) \cdot \varepsilon_0 \quad (10)$$

The function $\hat{\mathcal{J}}$, named *creep compliance*, and the function $\hat{\mathcal{K}}$, named *relaxation function* (Fung, 1993), specify the strain response to a unit step change in stress and the stress response to a unit step change in strain, respectively. In the following, similar to Wissler (2007), the stress response will be considered only. Nonetheless, as long as creep and relaxation phenomena are two aspects of the same viscoelastic behavior, the two functions $\hat{\mathcal{J}}$ and $\hat{\mathcal{K}}$ are related (Findley et al., 1989; Fung, 1993). By considering an imposed variable history of strain $\varepsilon(t)$ and by applying the superposition principle, from equation (10), the stress response is given by

$$\sigma_{ve}(t) = \int_0^t \hat{\mathcal{K}}(t - \tau) \cdot d[\varepsilon(\tau)] = \int_0^t \hat{\mathcal{K}}(t - \tau) \frac{d\varepsilon(\tau)}{d\tau} d\tau \quad (11)$$

having assumed $\varepsilon = 0$ for $t < 0$ and a differentiable strain history.

QLV model

When the linear hypothesis is not applicable, the need to overcome the difficulties of the nonlinear theory arises. In such a case, a QLV model, frequently used to describe the behavior of biological tissues, can be adopted in order to achieve a compromise between the simplicity of classical linear models and the difficulty of nonlinear approaches. According to the QLV hypothesis, as proposed by Fung (1993), the relaxation function is assumed to be of the form

$$\hat{\mathcal{K}}(\lambda, t) = \sigma_e(\lambda) \cdot g(t) \quad \text{with } g(0) = 1 \quad (12)$$

where $\sigma_e(\delta)$ is the *elastic response*, which is the amplitude of stress instantaneously generated by a stretch λ ,

whereas $g(t)$, called *reduced relaxation function*, describes the time-dependant behavior of the material. As for the nonlinear elastic response, it can be described, for instance, using an Ogden model of proper order (Findley et al., 1989). Under pure shear conditions of loading, the stress on the end plane of a rectangular EDF prestretched in the y -direction can be written as (Findley et al., 1989; Kofod, 2008)

$$\sigma_e = \sum_{p=1}^k \mu_p (\lambda_x^{\alpha_p} - \lambda_x^{-\alpha_p} \lambda_p^{-\alpha_p}) \quad (13)$$

where k is the model order and μ_p and α_p are material constitutive parameters.

As for the relaxation function $g(t)$, it is a decreasing continuous function of time, normalized to 1 at $t = 0$. It is customary to assume a linear combination of exponential functions, the exponents ν_i identifying the rate of the relaxation phenomena, and the coefficient c_i depending on the material

$$g(t) = \sum_{i=0}^r c_i e^{-\nu_i t} \quad \text{with} \quad \sum_{i=0}^r c_i = 1 \quad (14)$$

The parameters ν_i (for $i = 1, \dots, r$) depend on the system behavior, whereas $\nu_0 = 0$. The stress time history can be computed by means of the superposition principle (Fung, 1993). In particular, the stress produced by an infinitesimal change in stretch $d\lambda(\tau)$, superposed on a state of stretch λ at an instant of time τ , is, for $t > \tau$

$$d\sigma_{ve}(t) = g(t - \tau) \frac{\partial \sigma_e[\lambda(\tau)]}{\partial \lambda} d\lambda(\tau) \quad (15)$$

Finally, the total stress at the instant t is the sum of contributions of all the past changes (Findley et al., 1989), that is

$$\sigma_{ve}(t) = \int_0^t g(t - \tau) \frac{\partial \sigma_e[\lambda(\tau)]}{\partial \lambda} \frac{\partial \lambda(\tau)}{\partial \tau} d\tau \quad (16)$$

Physical insight of the QLV Model

In order to gain a better insight of the physical meaning of the QLV model, equation (16) can be rewritten in the form

$$\sigma_{ve}(t) = \int_0^t g(t - \tau) K_e[\lambda(\tau)] \dot{\lambda}(\tau) d\tau \quad (17)$$

where $K_e(\lambda) = \partial \sigma_e[\lambda] / \partial \lambda$. Recalling the *Zener model* illustrated in Figure 8, whose relaxation function \mathcal{K} is expressed by equation (10), the one-dimensional stress computed on the basis of equation (11) becomes

$$\sigma_{ve}(t) = \int_0^t \kappa_1 \left[\frac{\kappa_2}{\kappa_1 + \kappa_2} + \frac{\kappa_1}{\kappa_1 + \kappa_2} \cdot e^{-\frac{\kappa_1 + \kappa_2}{\eta}(t-\tau)} \right] \cdot \dot{\epsilon}(\tau) d\tau \quad (18)$$

On the other hand, for a nonlinear QLV material, by substituting equations (12) and (14) in equation (17), one obtains

$$\sigma_{ve}(t) = \int_0^t K_e(\lambda) \cdot \left[c_0 + \sum_{i=1}^r c_i e^{-\nu_i(t-\tau)} \right] \cdot \dot{\lambda}(\tau) d\tau \quad (19)$$

By noting that $\varepsilon = \lambda - 1$, a comparison between equations (19) and (18) reveals that the stress response of the QLV model can be interpreted as that of a nonlinear stiffness connected by a series of r linear Kelvin models, as illustrated in Figure 6(b) and in the BG of Figure 7.

QLV: from BG to block-scheme representation

As previously done in the study by Biagiotti et al. (2005), the QLV model can be usefully examined through a block-scheme representation. Equation (17) or (19) are interpreted considering the term $K_e(\lambda)\dot{\lambda}$ as a signal filtered by the linear system represented by

$$G(s) = \mathcal{L}\{g(t)\}$$

where \mathcal{L} denotes the Laplace transform. It is possible to find that the total force $\sigma_{ve}(t)$, induced by a displacement $\lambda(t)$, is given by two main additive contributions. The former term

$$\begin{aligned} \sigma_1(t) &= \mathcal{L}^{-1} \left\{ \frac{c_0}{s} \cdot L \left\{ \frac{\partial \sigma_e(\lambda)}{\partial \lambda} \cdot \dot{\lambda} \right\} \right\} \\ &= c_0 \int_0^t \frac{\partial \sigma_e(\lambda(\tau))}{\partial \lambda} \cdot \dot{\lambda} d\tau = c_0 \cdot \sigma_e[\lambda(t)] \end{aligned} \quad (20)$$

represents the elastic DE response in steady state, whereas the latter term

$$\sigma_2(t) = \mathcal{L}^{-1} \{ G_\sigma(s) \cdot L \{ K_e(\lambda) \cdot \dot{\lambda} \} \} \quad (21)$$

where

$$G_\sigma(s) = \frac{c_1}{s + \nu_1} + \dots + \frac{c_i}{s + \nu_i} + \dots + \frac{c_r}{s + \nu_r} \quad (22)$$

reproduces the time-dependent behavior of the material. In parallel, the term F_{ve} is composed of a purely elastic response F_1 , and a time-dependent response F_2 , and can be computed using equations (1) and (5)

$$F_{ve} = \underbrace{z'y'\lambda^{-1}\sigma_1}_{F_1} + \underbrace{z'y'\lambda^{-1}\sigma_2}_{F_2} \quad (23)$$

The corresponding block diagram is depicted in Figure 9.

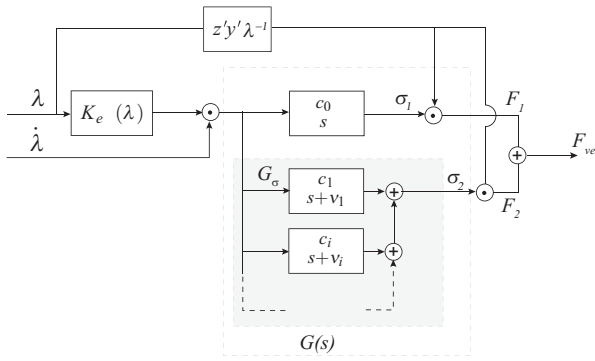


Figure 9. Block diagram of the quasi-linear model (Biagiotti et al., 2005). The function G_{σ} is composed of r blocks, see equation (22).

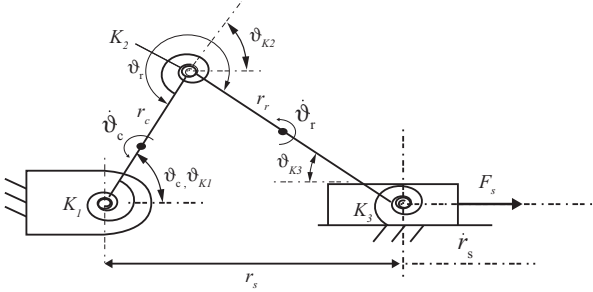


Figure 10. Compliant frame half model schematic.

Compliant frame model

Concerning the compliant mechanism representing the frame, a pseudo-rigid-body model of the system can be derived, according to analysis procedures as described in (Howell, 2001; Boyle et al., 2003). The compliant frame is modeled as a double SCCM (Figure 1(d)). Due to symmetry, half the frame can be modeled as a single SCCM (Figure 10).

Following the general methodology described in the study by Allen and Dubowsky (1977), let us define the ordered vector $\dot{\mathbf{q}}_k$ of generalized velocities (given with respect to the ground link)

$$\dot{\mathbf{q}}_k = [\dot{\mathbf{q}}_{kl} \mid \dot{\mathbf{q}}_{kd}]^t \quad (24)$$

$$\dot{\mathbf{q}}_{kl} = [\dot{r}_s]; \quad \dot{\mathbf{q}}_{kd} = [\dot{\vartheta}_c \ \dot{\vartheta}_r]^t \quad (25)$$

where, with reference to the BG of Figure 7, $\dot{\mathbf{q}}_{kl}$ is the chosen vector of independent flows and $\dot{\mathbf{q}}_{kd}$ is the vector of dependent flows. With reference to Figure 10, \dot{r}_s is the slider speed, whereas $\dot{\vartheta}_c$ and $\dot{\vartheta}_r$ are the crank and connecting-rod angular velocities, respectively. Hence, $\mathbf{q}_k = [\mathbf{q}_{kl} \mid \mathbf{q}_{kd}]^t = [r_s \mid \vartheta_c \ \vartheta_r]$ represents an ordered vector of generalized displacements.

Let us define, for notational convenience, $S_i = \sin \vartheta_i$, $S_{ij} = \sin(\vartheta_i - \vartheta_j)$, $C_i = \cos \vartheta_i$, and

$C_{ij} = \cos(\vartheta_i - \vartheta_j)$, the subscripts i and j varying according to the subscript of the function argument. From the displacement analysis of the mechanism, the following relationships are found

$$C_c = \frac{r_s^2 + r_c^2 - r_r^2}{2r_s r_c}; \quad S_r = -\frac{r_c}{r_r} S_c \quad (26)$$

From the velocity analysis of the mechanism, the relation between dependent and independent flows and static efforts is given by

$$\dot{\mathbf{q}}_{kd} = \mathbf{T}_k \dot{\mathbf{q}}_{kl} \quad (27)$$

$$\mathbf{e}_{kd} = \mathbf{T}_k^t \mathbf{e}_{kl} \quad (28)$$

$$\mathbf{T} = [\beta_c \ \beta_r]^t \quad (29)$$

having defined $\beta_c = (-r_c^2 S_c C_c / \xi - r_c S_c)^{-1}$, $\beta_r = -v_c r_c C_c / \xi$, and $\xi = (r_r^2 - r_c^2 S_c^2)^{1/2}$.

The inertias of SCCM crank and connecting rod are reasonably neglected. The inertia of the moving platform, also accounting for the EDF deforming masses, is described by an \mathbf{I}_s element with derivative causality. The effort e is simply given by

$$e_{\mathbf{I}_s} = \frac{m_s + m_{EAF}}{2} (\ddot{r}_s + g) \quad (30)$$

where m_s and m_{EAF} are SCCM slider mass and an equivalent mass describing the EDF deforming mass, whereas g is the acceleration of gravity. As for the frame stiffness, the compliance of SCCM joints is described by a compliance field \mathbf{C}_f with integral causality and constituted by three elements. With reference to Figure 7, the vector $\mathbf{v}_C \in \mathbb{R}^3$ of velocities related to the \mathbf{C}_f -field is given by

$$\mathbf{v}_C = [\dot{\vartheta}_{K1} \ \dot{\vartheta}_{K2} \ \dot{\vartheta}_{K3}]^t = \mathbf{T}_C \dot{\mathbf{q}}_k \quad (31)$$

The matrix \mathbf{T}_C is defined as

$$\mathbf{T}_C = \begin{bmatrix} 0 & 1 & 0 \\ 0 & 1 & -1 \\ 0 & 0 & 1 \end{bmatrix} \quad (32)$$

The efforts \mathbf{w}_C on the bonds of the \mathbf{C}_f -field are simply given by

$$\mathbf{w}_C = \mathbf{K}_f [\mathbf{v}_C - \mathbf{v}_{C0}] \quad (33)$$

where $\mathbf{K}_f = \text{diag}\{K_1, K_2, K_3\} \in \mathbb{R}^3$ is a diagonal matrix of (constant) joint stiffness coefficients, and $\mathbf{v}_{C0} = \mathbf{v}_C(t=0)$. The vector of efforts \mathbf{e}_C due to the compliance field \mathbf{C}_s can be computed as

$$\mathbf{e}_C = \mathbf{T}_C^t \mathbf{w}_C = \mathbf{T}_C^t \mathbf{K}_f [\mathbf{v}_C - \mathbf{v}_{C0}] \quad (34)$$

The term \mathbf{e}_C is partitioned into the following terms (see Figure 7)

$$\mathbf{e}_c = \begin{pmatrix} \mathbf{e}_{Cs} \\ \mathbf{e}_{Cm} \end{pmatrix} \quad (35)$$

where the subscript “s” refers to efforts associated with the SCCM slider and the subscript “m” refers to efforts associated with every other body of the mechanism.

Efforts on “1” junctions associated with the \mathbf{q}_k vector are given by

$$F_{SCCN} = f_s + e_{1s} + e_{Cs} \quad (36)$$

$$\mathbf{e}_{kl} = \mathbf{e}_{Cm} \quad (37)$$

Finally, by noting that two identical SCCM are connected to the same slider and by using equations (28) and (37) in equation (36), the overall frame force can be derived as

$$F_s = 2[\mathbf{T}'(\mathbf{e}_{Cm}) + e_{1s} + e_{Cs}] \quad (38)$$

Dissipative effects and the effect of the crank and slider inertias can be included by following the procedure described in the study by Allen and Dubowsky (1977). For the purpose of the present article, such inclusion seems unnecessary.

Elastic hinge design

The hinge physical dimensions can be calculated once joint stiffness coefficients, K_1, K_2 , and K_3 , have been designed. Referring to Figure 11, the bending stiffness of a single closed-wound helical spring has been evaluated in Lotti et al. (2006) and can be expressed as

$$k_i = 0.95 \frac{E}{2 + \nu} \frac{r^5}{Rl} \quad i = 1, 2, 3 \quad (39)$$

where D is the external spring diameter, d is the wire diameter ($r = d/2$ being the wire radius), $R = (D - d)/2$ is the mean helix radius, l is the coil length, and E and ν are the spring material Young’s modulus and Poisson’s ratio, respectively. Note that as depicted in Figure 3, two springs are used in parallel such that the overall joint stiffness can be computed as $K_i = 2k_i$.

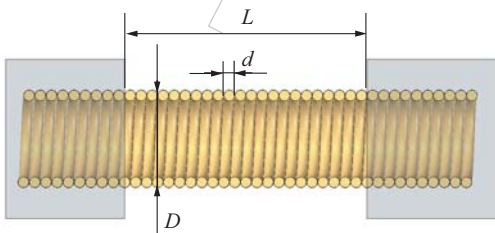


Figure 11. Close-wound spring hinge: basic parameters. Adapted from Lotti et al. (2006).

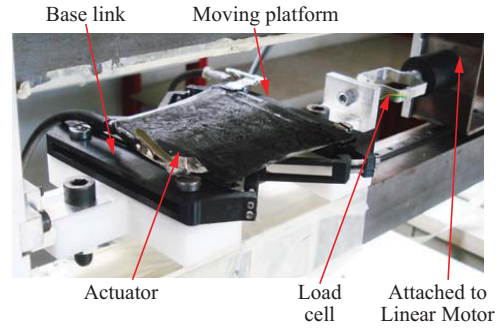


Figure 12. Experimental setup.

Numerical and experimental results

The adopted experimental setup is visible in Figure 12 and comprises a linear motor (Linmot P01-23 \times 80) equipped with a position sensor having 1 μm resolution. The motor slider is then directly connected to a load cell characterized by a structural stiffness of 242000 N/mm and accuracy of 0.1 N. Either the rectangular EDF specimen (Figure 5(b)) or the overall actuator (Figure 5(d)) is mounted such that the moving platform is rigidly connected to the load cell, whereas the base link is kept fixed. A general purpose digital signal processor (DSP) board is used to implement a basic position controller (with a sampling time of 1 ms) such that proper trajectories are applied to the platform and the normal component of the reaction force is continuously monitored.

Fitting of the model constants

The EDF used for the experimental validation is a membrane of an acrylic elastomer (VHB-4905), whereas the compliant electrodes are made with a conductive grease. At first, the specimen is preconditioned meaning that the rectangular EDF is subjected to mechanical and electrical loading–unloading cycles at constant velocity.

For the purpose of the present article, the specimen consisted of a virgin rectangular acrylic DE having initial dimensions $\bar{x} \times \bar{y} = 5 \times 33.3$ mm, which is pre-stretched in the y -direction ($\lambda_p = 3$), coated with conductive grease and glued to two identical rigid beams (i.e. the base link and the moving platform). The tensile test consisted in preliminary displacing the moving link from the length $x = \bar{x} = 5$ mm (initial length) to $x = 36$ mm, then cyclically displacing the same link between the length $x = 14$ mm and $x = 36$ mm at a constant velocity of 1 mm/s. At the same time, the EDF electrodes were subjected to an actuation voltage equaling $V = 0$ kV for the first eight cycles, $V = 3.0$ kV for the subsequent three cycles, and $V = 6.0$ kV for the last three cycles. In particular, Figure 13 highlights that the electromechanical response of typical rectangular EDFs features:

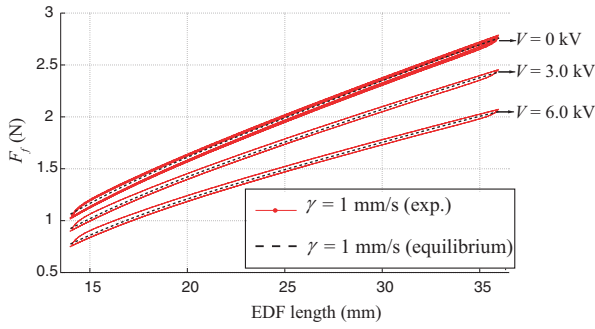


Figure 13. Experimental FL curve of a rectangular EDF specimen subjected to mechanical and electrical loading–unloading cycles (preconditioning). EDF: electrically deformable film; FL: force–length.

- A reduction in stress (stress softening) at a given strain on each successive loading, which is largest in the first loading–unloading cycle, becomes rather negligible after about three cycles and is rather insensitive to EDF electrical activation;
- Sensible difference between the loading and unloading forces (hysteresis) corresponding to the same deformation level, whose magnitude is rather insensitive to EDF electrical activation.

In addition, a residual strain (permanent set) is noticed, which is mostly generated during the first loading–unloading cycle and appears to reach a fixed value after about six cycles. After preconditioning, a specimen with initial length equaling \bar{x} is then characterized by an unloaded length $x > \bar{x}$ and a stabilized, repeatable behavior. The constants μ_p , α_p , v_i , and c_i can now be assessed by imposing a “ramp–hold” displacement history to the specimen (Figure 14).

The fitting procedure, described in, for example, the study of Berselli et al. (2011a), is composed of two steps:

- First, the specimen is displaced at an increasing speed $\dot{\lambda}$. A sufficiently high $\dot{\lambda} = \gamma^*$ is determined, upon which the time-dependent effects are negligible for application purposes (i.e. for $\dot{\lambda} \rightarrow \infty$, the response of the material is similar to that of an ideal step). This FL profile is taken as a good approximation of the purely elastic response F_1 (Figure 9) and can be used to determine μ_p and α_p by means of standard least-square fitting (Berselli et al., 2011a). A second-order Ogden model ($p = 2$; equation (13)) is chosen for material description, whereas γ^* is set to 10 mm/s.
- Once μ_p , α_p are known, the values for v_i , c_i are determined by minimizing the integral square error of the model output with respect to the experimental response

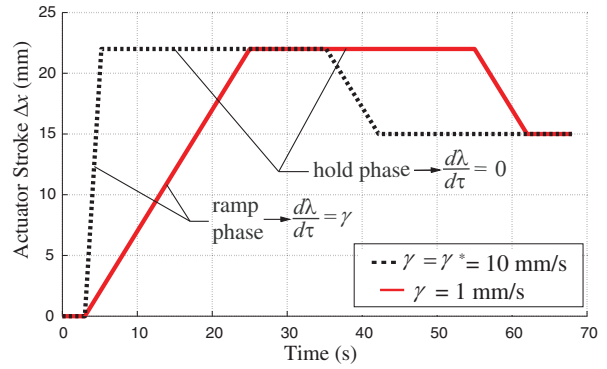


Figure 14. Trajectory of displacement used to first determine (ramp–hold test) and then validate the EDF model constants.

$$\min_{v_i, c_i} \int_0^{\infty} (F_{ve}(t) - \overline{F_{ve}}(t))^2 dt \quad (40)$$

where $\overline{F_{ve}}$ is the force of the real system (measured data), whereas F_{ve} is the model force. The integral is performed along the overall “ramp–hold” test, and a second-order reduced relaxation function ($r = 2$; equation (14)) is chosen for material description.

In order to assess the validity of the proposed viscoelastic model, a set of experimental tests is performed by, first, applying a predefined actuation voltage and, subsequently, displacing the moving link up to a maximum stroke of $\Delta x = 22$ mm, using five different rates of loading, γ , namely, $\gamma = 0.1, 0.5, 1, 5,$ and 10 mm/s. The maximum stroke is then held constant for 30 s, allowing the force response to stabilize, reduced to 15 mm at a speed of 1.00 mm/s, and finally held constant for another 30 s. As an instance, Figure 14 depicts two tests characterized by $\gamma = 1$ mm/s and $\gamma = \gamma^* = 10$ mm/s, respectively. The corresponding numerical and experimental force responses, for an actuation voltage equaling $V = 0$ kV, are depicted in Figure 15(a). In addition, Figure 15(b) reports the Maxwell force, F_{em} , concerning the same displacement time history for an actuation voltage equaling $V = 4$ kV. This same plot confirms that the Maxwell force (obtained by subtracting the force responses achieved for $V = 0$ kV and $V = 4$ kV, respectively) can be effectively modeled as a velocity-independent term as expressed in equation (7).

Overall actuator model: simulation and experimental validation

Numerical simulations are first run in order to correctly design the compliant frame. As for the EDF, the model parameters are reported in Table 1 and the contribution of gravity is neglected. The actuator is subjected to work cycles where the moving platform position $x = r_s$, velocity $\dot{x} = \dot{r}_s$, and acceleration $\ddot{x} = \ddot{r}_s$ are imposed by

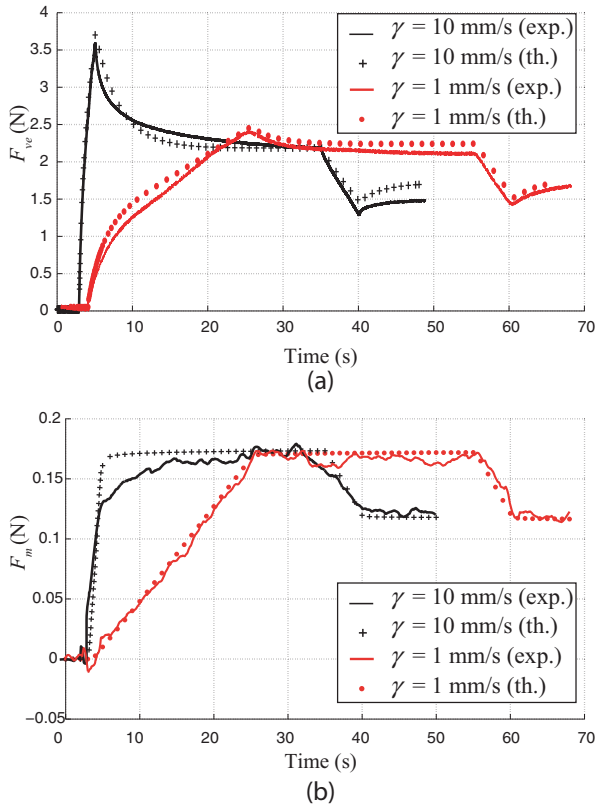


Figure 15. Time-histories of EDF forces F_{ve} and F_m . (a) EDF force F_{ve} response as a function of time when subjected to the displacement histories as shown in Figure 14 and (b) Maxwell force F_m response as a function of time when subjected to the displacement histories as shown in Figure 14. EDF: electrically deformable film.

an external user along with a voltage command V_B . Starting from the minimum actuator length, the position is increased (opening cycle), while a constant voltage is applied as a step function ($V_B = 6.0$ kV). When the maximum imposed position is reached, the output voltage is removed and the direction of imposed motion is reversed (closing cycle). Figure 16 reports qualitative time plots of the simulation variables imposed by an external user. Figure 17 reports the simulation results concerning the EDF force F_f during the opening and closing cycle for different velocity profiles (\dot{x}_{max} being the maximum velocity). The force difference between the opening and closing forces, ΔF_f , (Figure 17) corresponds to the *actuation force* that can be used to provide useful work to an outside system. The term ΔF_f

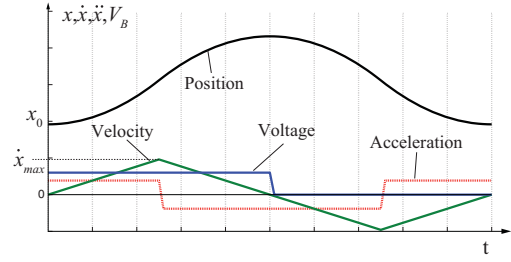


Figure 16. Qualitative time plots of voltage command V_B and moving platform position $x = r_s$, velocity $\dot{x} = \dot{r}_s$, and acceleration $\ddot{x} = \ddot{r}_s$.

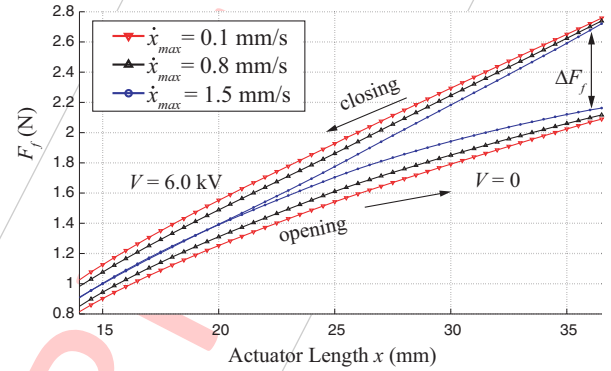


Figure 17. EDF force F_f as function of actuator length and maximum value of imposed velocity \dot{x}_{max} . EDF: electrically deformable film.

varies with both the actuator stroke and applied velocity. In particular, due to the viscoelastic nature of the DE, the actuation force decreases as the velocity increases, eventually vanishing at some stage.

Once the EDF FL curves are known, the compliant frame can be designed by means of the methodology previously described by the authors in the study of Berselli et al. (2011b), whereas the elastic joints are dimensioned by means of equation (39). Figure 18 shows the overall actuator available thrust $F_a = F_f + F_s$ (EDF + compliant frame) as compared to the sole EDF force, F_f . Both numerical and experimental values are reported. The overall frame parameters are reported in Table 2. The actuator thrust in the ON-state ($V = 6.0$ kV) is approximately constant

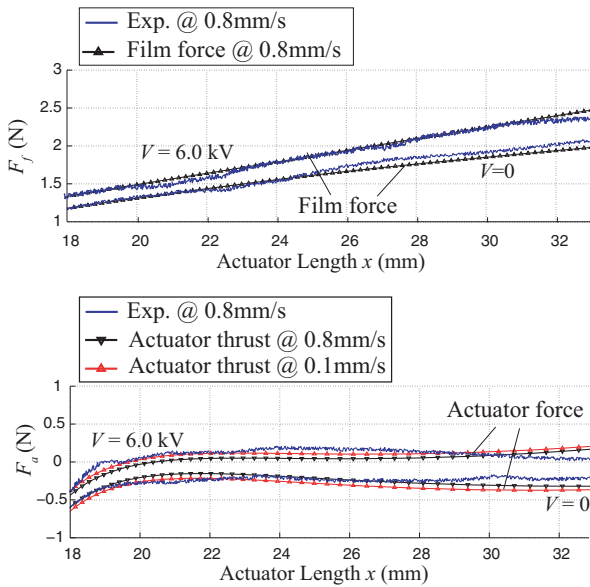
Table 1. EDF model parameters.

$x' = 14$ mm	$z' = 1.5$ mm	$y_p = 100$ mm	$\lambda_p = 3$ mm		
$c_0 = 0.4349$	$c_1 = 0.4347$	$c_2 = 0.1304$	$v_1 = 0.30$ s ⁻¹	$v_2 = 1.20$ s ⁻¹	
$\mu_1 = 18.952$ kPa	$\alpha_1 = 1.8$	$\mu_2 = 36.799$ kPa	$\alpha_2 = 1.9$	$R_E = 20$ k Ω	$R_I = 2.5$ G Ω

EDF: electrically deformable film.

Table 2. Frame parameters.

$r_c = 21.5 \text{ mm}$	$r_r = 35.7 \text{ mm}$	$m_s = 20 \text{ g}$	$m_{EAF} = 4 \text{ g}$	$\vartheta_{20} = 10^\circ$	$\vartheta_{30} = 173.9^\circ$
$E = 187.5 \text{ GPa}$	$\nu = 0.33$	$d = 0.4 \text{ mm}$	$D = 2.5 \text{ mm}$		
$K_1 = 5.80 \text{ N/mm}$	$l_1 = 9.0 \text{ mm}$	$K_2 = 7.80 \text{ N/mm}$	$l_2 = 6.0 \text{ mm}$	$K_3 = 8.05 \text{ N/mm}$	$l_3 = 5.8 \text{ N/mm}$

**Figure 18.** EDF force F_f and overall actuator force F_a . EDF: electrically deformable film.

(about 0 N) over the range 19–33 mm when the maximum imposed velocity equals 0.8 mm/s.

Conclusion

A hyperviscoelastic model of a constant-force DE actuator with rectangular shape has been presented. As for viscoelasticity, the quasi-linear framework has been adopted in order to achieve a compromise between the simplicity of classical linear models and the difficulty of nonlinear approaches. The model parameters have been determined by numerically fitting experimental data. As for the achievement of a constant-force output, the EDF has been coupled with a compliant frame designed, on the basis of the proposed simulations, in order to obtain a desired available thrust profile. As long as the overall actuator response is highly affected by time-dependent phenomena, the proposed model represents an important engineering tool when sizing the compliant frame parameters. Numerical simulations and experiments are provided, which validate the proposed modeling assumptions.

Funding

This research has been partially funded by InterMech MO.RE. Laboratory, Advanced Mechanics and Engine Design Research Center, Regione Emilia Romagna.

Acknowledgment

The authors wish to acknowledge the contribution of Dr Paolo Tiezzi.

Notes

- 1 The direction of vector \overline{OP} will be referred to as direction of actuation.
- 2 According to the definition given by Holzapfel (2001) a pure shear deformation is characterized by the constancy of one principal stretch (for instance λ_y). A pure shear deformation can be achieved for infinitely wide electrically deformable film (EDF), that is, for $y_p \gg x\sqrt{\Omega(t)}$, where $\Omega(t)$ are the possible configurations of the EDF in working condition.

References

- Allen R and Dubowsky S (1977) Mechanisms as components of dynamic systems: a bond graph approach. *Journal of Engineering for Industry* 99(1), 104–111.
- Babic M, Vertechy R, Berselli G, et al. (2010). An electronic driver for improving the open and closed loop electromechanical response of dielectric elastomer actuators. *Mechatronics* 20(2): 201–212.
- Berselli G, Piccinini M and Vassura G (2011a) Engineering design of fluid-filled soft covers for robotic contact interfaces: guidelines, nonlinear modeling, and experimental validation. *IEEE Transactions on Robotics* 27(3): 436–449.
- Berselli G, Vertechy R, Babic M, et al. (2012). Implementation of variable stiffness actuators based on dielectric elastomers: a feasibility study. In: *Proceedings of ASME SMASIS 2012 international conference on smart materials, adaptive structures and intelligent systems*, Stone Mountain, GA, USA, 19–21 September, pp. 1–10. ASME.
- Berselli G, Vertechy R, Vassura G, et al. (2009). Design of a single-acting constant-force actuator based on dielectric elastomers. *ASME Journal of Mechanisms and Robotics* 2: 391–398.
- Berselli G, Vertechy R, Vassura G, et al. (2011b) Optimal synthesis of conically shaped dielectric elastomer linear actuators: design methodology and experimental validation. *IEEE/ASME Transactions on Mechatronics* 16(1): 67–79.
- Biagiotti L, Melchiorri C, Tiezzi P, et al. (2005). Modelling and identification of soft pads for robotic hands. In: *Proceedings of IEEE/RSJ IROS, international conference on intelligent robots and systems*, Edmonton, AB, Canada, 2–6 August, pp. 2786–2791. IEEE.
- Bicchi A, Bavaro M, Boccadamo G, et al. (2008). Physical human-robot interaction: dependability, safety, and performance. In: *Proceedings of the 10th IEEE international workshop on advanced motion control*, Trento, Italy, 26–28 March, pp. 9–16. IEEE.
- Biddiss E and Chaua T (2007) Dielectric elastomers as actuators for upper limb prosthetics: challenges and opportunities. *Medical Engineering and Physics* 30: 403–418.

- Boyle C, Howell LL, Magleby SP, et al. (2003). Dynamic modeling of compliant constant-force compression mechanisms. *Mechanism and Machine Theory* 38(12): 1469–1487.
- Carpi F, Rossi DD, Kornbluh R, et al. (2008). *Dielectric Elastomers as Electromechanical Transducers*. New York: Elsevier.
- Dastoor S and Cutkosky M (2012). Design of dielectric electroactive polymers for a compact and scalable variable stiffness device. In: *Proceedings of IEEE ICRA, international conference on robotics and automation*, St. Paul, MN, USA, 14–18 May, pp. 1–6. IEEE.
- Findley WN, Lai JS and Onaran K (1989) *Creep and Relaxation of Nonlinear Viscoelastic Materials: With an Introduction to Linear Viscoelasticity*. New York: Dover Publications.
- Fung YC (1993) *Biomechanics: Mechanical Properties of Living Tissues*. Berlin: Springer-Verlag.
- Goulbourne N, Mockensturm E and Frecker M (2007). Electro-elastomers: large deformation analysis of silicone membranes. *International Journal of Solids and Structures* 44(9): 2609–2626.
- Hackl C, Tang H and Lorenzh R (2005) A multidomain model of planar electro-active polymer actuators. *IEEE Transactions on Industry Applications* 41(5): 1142–1148.
- Holzappel GA (2001) *Nonlinear Solid Mechanics: A Continuum Approach for Engineering*. New York: John Wiley and Sons.
- Howell L (2001) *Compliant Mechanisms*. New York: John Wiley and Sons.
- Huber JE, Fleck NA and Ashby M (1997) The selection of mechanical actuators based on performance indices. *Proceedings of the Royal Society of London, Series A* 453: 2185–2205.
- Kaal W and Herold S (2011) Electroactive polymer actuators in dynamic applications. *IEEE/ASME Transactions on Mechatronics* 16(1): 24–32.
- Karnopp D, Margolis D and Rosenberg R (2005) *System Dynamics. Modeling and Simulation of Mechatronic Systems*. 4th ed. New York: John Wiley and Sons.
- Kim L and Tadokoro S (2007) *Electroactive Polymers for Robotic Applications*. Berlin: Springer.
- Kofod G (2008) The static actuation of dielectric elastomer actuators: how does pre-stretch improve actuation? *Journal of Physics D: Applied Physics* 41: 215405.
- Kornbluh R, Pelrine R and Joseph J (1995) Dielectric artificial muscle actuators for small robots. In: *Proceedings of the IASTED International Conference on Robotics and Manufacturing*, Cancun, Mexico, 14–17 June.
- Lotti F, Zucchelli A, Reggiani B, et al. (2006) Evaluating the flexural stiffness of compliant hinges with close-wound helical springs. In: *Proceedings of DETC06, ASME design engineering technical conferences*, Philadelphia, PA, USA, 10–13 September.
- Michel S, Zhang X, Wissler M, et al. (2010) A comparison between silicone and acrylic elastomers as dielectric materials in electroactive polymer actuators. *Polymer International* 59(3): 391–399.
- Ogden RW (1972) Large deformation isotropic elasticity: on the correlation of theory and experiment for incompressible rubber-like solids. *Proceedings of the Royal Society of London Series A: Mathematical and Physical Sciences* 326: 565–584.
- O'Halloran A, O'Malley F and McHugh P (2008) A review on dielectric elastomer actuators, technology, applications, and challenges. *Journal of Applied Physics* 104(7): 071101.
- Palli G, Berselli G, Melchiorri C, et al. (2011). Design of a variable stiffness actuator based on flexures. *Journal of Mechanisms and Robotics* 3(3): 034501(5).
- Palli G and Melchiorri C (2011) Output-based control of robots with variable stiffness actuation. *Journal of Robotics* 2011: 735407.
- Pedersen C, Fleck N and Ananthasuresh G (2006) Design of a compliant mechanism to modify an actuator characteristic to deliver a constant output force. *Journal of Mechanical Design* 128(5): 1101–1112.
- Pelrine R, Kornbluh R and Joseph J (1998) Electrostriction of polymer dielectrics with compliant electrodes as a means of actuation. *Sensors Actuators A: Physical* 64: 77–85.
- Plante JS and Dubowsky S (2007) On the properties of dielectric elastomer actuators and their design implications. *Smart Materials and Structures* 16(2): 227–236.
- Rodriguez-Fortun J, Orus J, Buil F, et al. (2010) General bond graph model for piezoelectric actuators and methodology for experimental identification. *Mechatronics* 20: 303–314.
- Vertechy R, Berselli G, Bergamasco M, et al. (in press) Continuum thermo-electro-mechanical model for electrostrictive elastomers. *Journal of Intelligent Material Systems and Structures*. DOI: 10.1177/1045389X12455855.
- Vertechy R, Berselli G, Parenti Castelli, V, et al. (2010) Optimal design of lozenge-shaped dielectric elastomer linear actuators: mathematical procedure and experimental validation. *Journal of Intelligent Material Systems and Structures* 21: 503–515.
- Wingert A, Lichter MD and Dubowsky S (2006) On the design of large degree-of-freedom digital mechatronic devices based on bistable dielectric elastomer actuators. *IEEE/ASME Transactions on Mechatronics* 11(4): 448–456.
- Wissler MT (2007) *Modeling dielectric elastomer actuators*. PhD Thesis, Federal Institute of Technology, Zurich, Switzerland.
- Xie SQ, Ramson PF, Graaf DD, et al. (2005) An adaptive control system for dielectric elastomers. In: *IEEE International Conference on Industrial Technology*, 14–17 December 2005, pp. 335–340. IEEE.
- Zhang R, Kunz A, Lochmatter P, et al. (2006) Dielectric elastomer spring roll actuators for a portable force feedback device. In: *Symposium on haptic interfaces for virtual environment and teleoperator systems*, Arlington, VA, USA, 25–26 March, pp. 253–347. IEEE.